

# Statistical hadronization model approach to $\sqrt{s_{NN}} = 200$ GeV Au-Au collisions: $p_T$ -spectra fits and global variable predictions

Dariusz Prorok\*

*Institute of Theoretical Physics, University of Wrocław, Pl. Maksa Borna 9, PL-50-204 Wrocław, Poland*  
(Received 18 September 2006; revised manuscript received 28 November 2006; published 10 January 2007)

Three possible scenarios of the statistical hadronization model are reexamined with the use of the  $p_T$  spectra of the PHENIX and very low  $p_T$  PHOBOS measurements at  $\sqrt{s_{NN}} = 200$  GeV. These scenarios are as follows: (a) full chemical nonequilibrium, (b) strangeness chemical nonequilibrium, and (c) chemical equilibrium. Fits to the spectra are done within the Cracow single-freeze-out model, which takes into account both the expansion and resonance decays. Predictions for spectra of  $\phi$ ,  $K(892)^{*0}$ , and  $\pi^0$  are also given. Global variables such as the transverse energy at midrapidity, the charged particle multiplicity at midrapidity, and the total multiplicity of charged particles are evaluated and their predicted values agree qualitatively well with the experimental data. The thorough analysis within this model suggests that the chemical full nonequilibrium case is the least likely and both other cases are of similar likelihood. It is also shown that if the full chemical nonequilibrium freeze-out took place it could manifest itself in the enhancement of the  $\pi^0$  production at very low transverse momenta.

DOI: [10.1103/PhysRevC.75.014903](https://doi.org/10.1103/PhysRevC.75.014903)

PACS number(s): 25.75.Dw, 24.10.Pa, 24.10.Jv

## I. INTRODUCTION

Since the first run of the Relativistic Heavy Ion Collider (RHIC) a vast amount of data on hadron production from the hot and dense fireball created in a collision has been available. In this paper the application of the statistical hadronization model (SHM) to the description of the fireball bulk properties [1] is re-examined with the use of the  $p_T$  spectra measured by the PHENIX Collaboration at the top RHIC energy  $\sqrt{s_{NN}} = 200$  GeV [2].

In the SHM the formation process of each particle is described on the basis of the assumption that the accessible phase space is fully saturated (maximized). Then the particle yields are determined by their phase-space weight, which is given by a statistical distribution. (For a comprehensive review of the model see Ref. [3].) The main feature of this model is that it allows deviation from the usually presumed chemical equilibrium of the fireball at freeze-out. This has been achieved via the introduction of some new parameters, so-called phase-space occupancy factors:  $\gamma_q$  for light quarks and  $\gamma_s$  for strange quarks in hadrons. In Ref. [1] three possible cases were considered:

- (i) full chemical nonequilibrium,  $\gamma_q \neq 1$ ,  $\gamma_s \neq 1$ ;
- (ii) strangeness chemical nonequilibrium (semi-equilibrium),  $\gamma_q = 1$ ,  $\gamma_s \neq 1$ ; and
- (iii) chemical equilibrium,  $\gamma_q = 1$ ,  $\gamma_s = 1$ .

The phase-space occupancy factors  $\gamma_q$  and  $\gamma_s$  together with the temperature  $T$  and baryon number chemical potential  $\mu_B$  comprise the full set of independent statistical parameters of the model. For all three cases of chemical nonequilibrium/equilibrium, values of these parameters have been determined in Ref. [1]. This was done for each centrality bin of the PHENIX measurement at  $\sqrt{s_{NN}} = 200$  GeV from fits to the PHENIX identified hadron yields [2] complemented

with  $K^*(892)/K^-$  and  $\phi/K^-$  ratios measured by the STAR Collaboration [4–6].

However, the possible expansion of the fireball is invisible in particle yield ratios (since a collective flow is able to modify only the momentum spectra of a measured particle, but not its multiplicity). Therefore, in addition to the studies of particle ratios the analysis of the  $p_T$  spectra is necessary to gain some quantitative information about the flow. Such an analysis was done for the chemical equilibrium case of the SHM (the third point of the preceding list) in Ref. [7]. In the present paper a similar analysis of the  $p_T$  spectra will be performed for both chemical nonequilibrium cases of the SHM (the first and the second points of the preceding list).

To describe the flow at the freeze-out stage, the single-freeze-out model of Refs. [8–10] is applied. The model succeeded in the accurate description of ratios and  $p_T$  spectra of particles measured at RHIC. The main postulate of the model is the simultaneous occurrence of chemical and thermal freeze-outs, which means that possible elastic interactions after the chemical freeze-out are neglected. The conditions for the freeze-out are expressed by values of two independent thermal parameters:  $T$  and  $\mu_B$ . The second basic feature of the model is the complete treatment of resonance decays. This means that the final distribution of a given particle consists not only of the thermal part but also of contributions from all possible decays and cascades. Feeding from weak decays is included as well. Since in the original formulation [8–10] this model corresponds to the chemical equilibrium case of the SHM, the single-freeze-out model will be generalized to chemical nonequilibrium cases of the SHM in the present paper.

Global variables such as the transverse energy at midrapidity ( $dE_T/d\eta|_{\text{mid}}$ ), the charged particle multiplicity at midrapidity ( $dN_{\text{ch}}/d\eta|_{\text{mid}}$ ), and the total multiplicity of charged particles ( $N_{\text{ch}}$ ) are also evaluated for both chemical nonequilibrium cases of the SHM for different centrality bins of the PHENIX measurements at  $\sqrt{s_{NN}} = 200$  GeV [11]. These three variables are independent observables, which means

\*Electronic address: prorok@ift.uni.wroc.pl

that they are measured independently of identified hadron spectroscopy. Because model fits were done to identified hadron data (particle yield ratios and  $p_T$  spectra) and the global variables are calculable in the generalized single-freeze-out model, it was natural to check whether their estimated values agree with the data. This has proven to be true within 10% accuracy. It should be stressed also here that the centrality independence of the total multiplicity of charged particles per participant pair has been reproduced. The evidence for such scaling of the total multiplicity was reported by the PHOBOS Collaboration [12].

In some sense this work could be understood as an additional test of the correctness of the determination of the statistical parameters of the SHM since these parameters enter primordial distributions of hadrons in the fireball at freeze-out. Thus fits of geometric parameters of the generalized single-freeze-out model are done with the use of the values of the statistical parameters obtained earlier in Ref. [1] and treated as input here. The general conclusion is that the best-quality fits to the  $p_T$  spectra of identified hadrons are obtained for the strangeness chemical nonequilibrium case of the SHM. What is surprising is that in the chemical equilibrium case the spectra seem to be fitted better than in the scenario with full chemical nonequilibrium. Whenever the term “strangeness chemical nonequilibrium case” or “full chemical nonequilibrium case” is used in this paper it means the case with its values of statistical parameters taken from Ref. [1] and listed in Table I (Sec. IV A). Additionally, the spectra of  $\phi$  and  $K(892)^{*0}$  resonances are predicted. In this way the spectra of each particle species whose yield was used to determine the statistical parameters of the model [1] are calculated. Also the measurement of the low-momentum  $\pi^0$  is proposed as a test, which could help to ascertain whether the full chemical nonequilibrium could happen in the fireball at freeze-out. Namely, values of  $\gamma_q$  determined in Ref. [1] cause the predictions for low- $p_T$   $\pi^0$  to be about 40% greater in this case than in semi-equilibrium or equilibrium cases.

## II. THE SINGLE-FREEZE-OUT MODEL AND ITS GENERALIZATION

The main assumptions of the model are as follows: (a) Chemical and thermal freeze-outs take place simultaneously, (b) all confirmed resonances up to a mass of 2 GeV from the Particle Data Tables [13] are taken into account, (c) a freeze-out hypersurface is defined by the equation

$$\tau = \sqrt{t^2 - r_x^2 - r_y^2 - r_z^2} = \text{const}, \quad (1)$$

(d) the four-velocity of an element of the freeze-out hypersurface is proportional to its coordinate

$$u^\mu = \frac{x^\mu}{\tau} = \frac{t}{\tau} \left( 1, \frac{r_x}{t}, \frac{r_y}{t}, \frac{r_z}{t} \right), \quad (2)$$

and (e) the following parametrization of the hypersurface is chosen:

$$\begin{aligned} t &= \tau \cosh \alpha_{\parallel} \cosh \alpha_{\perp}, & r_x &= \tau \sinh \alpha_{\perp} \cos \phi, \\ r_y &= \tau \sinh \alpha_{\perp} \sin \phi, & r_z &= \tau \sinh \alpha_{\parallel} \cosh \alpha_{\perp}, \end{aligned} \quad (3)$$

where  $\alpha_{\parallel}$  is the rapidity of the element,  $\alpha_{\parallel} = \tanh^{-1}(r_z/t)$ , and  $\alpha_{\perp}$  controls the transverse radius, given by

$$\rho = \sqrt{r_x^2 + r_y^2} = \tau \sinh \alpha_{\perp} < \rho_{\max}, \quad (4)$$

where the restriction on the transverse size has been introduced, so that  $\rho_{\max}$  gives the maximal transverse extension of the gas in the central slice during the freeze-out. This means that two new parameters of the model have been introduced (i.e.,  $\tau$  and  $\rho_{\max}$ ), which are connected with the geometry of the freeze-out hypersurface.

From Eq. (1) one can see that the beginning of the freeze-out process starts at  $t_{\text{f.o.}}^{(1)} = \tau$  and  $\vec{r} = 0$  in the c.m. system, which is also the laboratory frame in the RHIC case. At this moment the volume of the gas can be estimated as

$$V_{\text{f.o.}}^{(1)} = 2\pi\tau\rho_{\max}^2, \quad (5)$$

which is simply the volume of a tube with a length  $2\tau$  and a radius  $\rho_{\max}$  (where  $2\tau$  is the maximal possible extension of the gas in the longitudinal direction at  $t_{\text{f.o.}}^{(1)}$ ). In the central slice the freeze-out ceases at  $t_{\text{f.o.}}^{(2)} = \sqrt{\tau^2 + \rho_{\max}^2}$  and it takes place at  $\rho = \rho_{\max}$ .

The transverse velocity in the central slice can be expressed as a function of the transverse radius

$$\beta_{\perp}(\rho) = \tanh \alpha_{\perp} = \frac{\rho}{\sqrt{\tau^2 + \rho^2}}. \quad (6)$$

The maximum value of  $\beta_{\perp}$ , called the maximum transverse-flow parameter (or the surface velocity), is given by

$$\beta_{\perp}^{\max} = \frac{\rho_{\max}}{\sqrt{\tau^2 + \rho_{\max}^2}} = \frac{\rho_{\max}/\tau}{\sqrt{1 + (\rho_{\max}/\tau)^2}}. \quad (7)$$

The invariant distribution of the measured particles of species  $i$  has the form [8,9]

$$\frac{dN_i}{d^2p_T dy} = \int p^\mu d\sigma_\mu f_i(p \cdot u), \quad (8)$$

where  $d\sigma_\mu$  is the normal vector on a freeze-out hypersurface,  $p \cdot u = p^\mu u_\mu$ ,  $u_\mu$  is the four-velocity of a fluid element, and  $f_i$  is the final momentum distribution of the particle in question. The final distribution means here that  $f_i$  is the sum of primordial and simple and sequential decay contributions to the particle distribution (for details see Refs. [10,14]).

For the most general case of the chemical nonequilibrium the primordial momentum distribution of particle species  $i$  is given by

$$f_i^{\text{primordial}} = \frac{(2s_i + 1)}{(2\pi\hbar c)^3} \frac{1}{\gamma_i^{-1} \exp\left\{\frac{E_i - \mu_i}{T}\right\} + g_i}, \quad (9)$$

where  $E_i = (m_i^2 + p^2)^{1/2}$  and  $m_i$ ,  $\mu_i$ ,  $s_i$ , and  $g_i$  are the mass, chemical potential, spin, and a statistical factor of species  $i$ ,

respectively. The chemical potential  $\mu_i = B_i\mu_B + S_i\mu_S + I_3^i\mu_{I_3}$ , where  $B_i$ ,  $S_i$ , and  $I_3^i$  are the baryon number, strangeness, and the third component of the isospin of the particle species in question, whereas  $\mu$ 's are the corresponding overall chemical potentials. The strangeness chemical potential  $\mu_S$  is determined from the requirement that the overall strangeness equals zero. The chemical potential related to the third component of the isospin,  $\mu_{I_3}$ , is derived from the constraint that the charge to the net baryon ratio in the final state is the same as in the colliding nuclei. It has turned out that  $\mu_{I_3}$  is negligible at RHIC ( $|\mu_{I_3}| \leq 1$  MeV [1,10]), so it will be omitted in further considerations. The nonequilibrium factor  $\gamma_i$  reads

$$\gamma_i = \gamma_q^{(N_q^i + N_{\bar{q}}^i)} \gamma_s^{(N_s^i + N_{\bar{s}}^i)}, \quad (10)$$

where  $\gamma_{q(s)}$  is the light (strange) quark phase-space occupancy factor,  $N_q^i$  and  $N_s^i$  are the numbers of light and strange quarks in the  $i$ th hadron, and  $N_{\bar{q}}^i$  and  $N_{\bar{s}}^i$  are the numbers of the corresponding antiquarks in the same hadron.

With the use of Eqs. (2) and (3), the invariant distribution (8) takes the following form:

$$\begin{aligned} \frac{dN_i}{d^2p_T dy} &= \int d\sigma(p \cdot u) f_i(p \cdot u) \\ &= \tau^3 \int_{-\infty}^{+\infty} d\alpha_{\parallel} \int_0^{\rho_{\max}/\tau} \sinh\alpha_{\perp} d(\sinh\alpha_{\perp}) \\ &\quad \times \int_0^{2\pi} d\xi (p \cdot u) f_i(p \cdot u), \end{aligned} \quad (11)$$

where

$$p \cdot u = m_T \cosh(\alpha_{\parallel} - y) \cosh\alpha_{\perp} - p_T \cos\xi \sinh\alpha_{\perp}. \quad (12)$$

### III. TRANSVERSE ENERGY AND CHARGED PARTICLE MULTIPLICITY

The experimentally measured transverse energy is defined as

$$E_T = \sum_{i=1}^L \hat{E}_i \cdot \sin\theta_i, \quad (13)$$

where  $\theta_i$  is the polar angle,  $\hat{E}_i$  denotes  $E_i - m_N$  (with  $m_N$  the nucleon mass) for baryons,  $E_i + m_N$  for antibaryons and the total energy  $E_i$  for all other particles, and the sum is taken over all  $L$  emitted particles [11].

The pseudorapidity density of particle species  $i$  is given by

$$\begin{aligned} \frac{dN_i}{d\eta} &= \int d^2p_T \frac{dy}{d\eta} \frac{dN_i}{d^2p_T dy} \\ &= \int d^2p_T \frac{p}{E_i} \frac{dN_i}{d^2p_T dy}. \end{aligned} \quad (14)$$

Analogously, the transverse energy pseudorapidity density for the same species can be written as

$$\begin{aligned} \frac{dE_{T,i}}{d\eta} &= \int d^2p_T \hat{E}_i \cdot \frac{p_T}{p} \frac{dy}{d\eta} \frac{dN_i}{d^2p_T dy} \\ &= \int d^2p_T p_T \frac{\hat{E}_i}{E_i} \frac{dN_i}{d^2p_T dy}. \end{aligned} \quad (15)$$

For the quantities at midrapidity one has (in the c.m. system, which is the RHIC case)

$$\left. \frac{dN_i}{d\eta} \right|_{\text{mid}} = \int d^2p_T \frac{p_T}{m_T} \frac{dN_i}{d^2p_T dy}, \quad (16)$$

$$\left. \frac{dE_{T,i}}{d\eta} \right|_{\text{mid}} = \begin{cases} \int d^2p_T p_T \frac{m_T - m_N}{m_T} \frac{dN_i}{d^2p_T dy}, & i = \text{baryon} \\ \int d^2p_T p_T \frac{m_T + m_N}{m_T} \frac{dN_i}{d^2p_T dy}, & i = \text{antibaryon} \\ \int d^2p_T p_T \frac{dN_i}{d^2p_T dy}, & i = \text{others.} \end{cases} \quad (17)$$

The overall charged particle and transverse energy densities can be expressed as

$$\left. \frac{dN_{\text{ch}}}{d\eta} \right|_{\text{mid}} = \sum_{i \in B} \left. \frac{dN_i}{d\eta} \right|_{\text{mid}}, \quad (18)$$

$$\left. \frac{dE_T}{d\eta} \right|_{\text{mid}} = \sum_{i \in A} \left. \frac{dE_{T,i}}{d\eta} \right|_{\text{mid}}, \quad (19)$$

where  $A$  and  $B$  ( $B \subset A$ ) denote sets of species of finally detected particles, namely the set of charged particles  $B = \{\pi^+, \pi^-, K^+, K^-, p, \bar{p}\}$ , whereas  $A$  also includes photons,  $K_L^0$ ,  $n$ , and  $\bar{n}$  [15].

The total multiplicity of particle species  $i$  can be also derived (for the more formal proof see [10]):

$$\begin{aligned} N_i &= \int d^2p_T dy \frac{dN_i}{d^2p_T dy} \\ &= \int d^2p_T dy \int p^\mu d\sigma_\mu f_i(p \cdot u) \\ &= \int d\sigma \int d^2p_T dy (p \cdot u) f_i(p \cdot u) \\ &= \int d\sigma \int \frac{d^3\vec{p}}{E} (p \cdot u) f_i(p \cdot u) \\ &= \int d\sigma n_i(T, \mu_B, \gamma_s, \gamma_q) \\ &= n_i(T, \mu_B, \gamma_s, \gamma_q) \int d\sigma, \end{aligned} \quad (20)$$

for any expansion satisfying the condition  $d\sigma_\mu \sim u_\mu$  on a freeze-out hypersurface and if the local statistical parameters are constant on this hypersurface (in the present model both conditions are fulfilled). Note that the density of particle species  $i$ ,  $n_i$ , includes thermal and decay contributions.

In practice the rapidity of the fluid element  $\alpha_{\parallel}$  should not be unlimited but should have its maximal value  $\alpha_{\parallel}^{\max}$ . Otherwise, the hypersurface volume and the total charged particle multiplicity would be infinite. Then one can express the hypersurface volume as

$$\begin{aligned} \int d\sigma &= \tau^3 \int_{-\alpha_{\parallel}^{\max}}^{+\alpha_{\parallel}^{\max}} d\alpha_{\parallel} \int_0^{\rho_{\max}/\tau} \sinh\alpha_{\perp} d(\sinh\alpha_{\perp}) \int_0^{2\pi} d\xi \\ &= 2\pi \alpha_{\parallel}^{\max} \tau \rho_{\max}^2. \end{aligned} \quad (21)$$

Finally, the total multiplicity of charged particles can be obtained:

$$\begin{aligned} N_{\text{ch}} &= 2\pi \alpha_{\parallel}^{\max} \tau \rho_{\max}^2 \sum_{i \in B} n_i(T, \mu_B, \gamma_s, \gamma_q) \\ &= 2\pi \alpha_{\parallel}^{\max} \tau \rho_{\max}^2 n_{\text{ch}}(T, \mu_B, \gamma_s, \gamma_q). \end{aligned} \quad (22)$$

For  $\alpha_{\parallel}^{\max}$  the following reasonable assumption has been made: It is equal to the rapidity of leading baryons after the collision. This means that the fluid that has been created in the central rapidity region (CRR) could not move faster in the longitudinal direction than fragments of a target or a projectile after the collision. Therefore  $\alpha_{\parallel}^{\max}$  should depend on the centrality of the collision, since the more central the collision is, the higher degree of the stopping of the initial baryons ought to happen in principle. There are two limiting cases: (i) the most central collision, where maximum stopping occurs, and (ii) when the centrality approaches 100%, when the stopping disappears. Assuming additionally that  $\alpha_{\parallel}^{\max}$  is a linear function of the centrality, we can derive the following parametrization (for details see Ref. [7]):

$$\alpha_{\parallel}^{\max}(c) = y_p - \frac{\langle \delta y \rangle}{0.975} \cdot (1 - c), \quad (23)$$

where  $y_p$  is the projectile rapidity,  $\langle \delta y \rangle$  is the average rapidity loss, and  $c$  is a fractional number representing the middle of a given centrality bin (i.e.,  $c = 0.025$  for the 0–5% centrality bin,  $c = 0.075$  for the 5–10% centrality bin, etc. The BRAHMS Collaboration reports  $\langle \delta y \rangle = 2.05$  for the 5% most central collisions at  $\sqrt{s_{NN}} = 200$  GeV ( $y_p = 5.36$ ) [16].

## IV. RESULTS

### A. Determination of geometric parameters

The determination of parameters of the model proceeds in two steps. First, statistical parameters  $T$ ,  $\mu_B$ ,  $\gamma_q$ , and  $\gamma_s$  are fitted with the use of the experimental ratios of hadron multiplicities at midrapidity. This has been already done in Ref. [1] for all available centrality bins of the PHENIX measurements at  $\sqrt{s_{NN}} = 200$  GeV [2]. Having put values of these parameters into the theoretical expression for the invariant distribution, Eqs. (11) and (12), the two remaining parameters  $\rho_{\max}$  and  $\tau$  can be determined from the simultaneous fit to the transverse-momentum spectra of  $\pi^{\pm}$ ,  $K^{\pm}$ ,  $p$ , and  $\bar{p}$ . The fits are performed with the help of the  $\chi^2$  method.

The final results for the geometric parameters  $\rho_{\max}$  and  $\tau$  are gathered in Table I together with the corresponding values

of  $\chi^2/\text{NDF}$  for each centrality class additionally characterized by the number of participants,  $N_{\text{part}}$ . The results are given for all three cases of the SHM listed in Sec. I (for comparison the results for the chemical equilibrium case are repeated from Ref. [7]). Other physical quantities such as the surface velocity  $\beta_{\perp}^{\max}$ , the volume at the beginning of freeze-out,  $V_{\text{f.o.}}^{(1)}$ , and the maximal freeze-out time at the central slice  $t_{\text{f.o.}}^{(2)}$  are also given there. Values of  $\rho_{\max}$  and  $\tau$  (therefore also  $V_{\text{f.o.}}^{(1)}$  and  $t_{\text{f.o.}}^{(2)}$ ) obtained in the case of full chemical nonequilibrium are substantially lower than corresponding values in both other cases. This is because  $\gamma_s$  and  $\gamma_q$  are significantly greater than 1 in this case, so primordial densities given by Eqs. (9) and (10) are also greater than in both other cases. And since fits are done to the same spectra, to keep the normalization unchanged, values of the geometric parameters have to decrease.

Except for the last three rows of Table I, all fits have been done with the use of the  $p_T$  spectra of identified charged hadrons measured by the PHENIX Collaboration in  $\sqrt{s_{NN}} = 200$  GeV Au-Au collisions [2,17]. Centrality classes with footnote marks denote two bins for which fitted spectra are taken from Ref. [17]. These are 0–10% and 10–40% centrality bins and they are not included in Ref. [2], so values of the statistical parameters have not been fitted for them in Ref. [1]. But for these bins  $\phi$  meson spectra have been reported in Ref. [17]. Thus to make predictions for  $\phi$  spectra, values of the statistical parameters have been taken as the averages of the values fitted for bins whose added percent coverage equals 0–10% or 10–40%. The last three rows of Table I present results of fits to the PHENIX data complemented with the low- $p_T$  data for  $\pi^{\pm}$  extracted from the PHOBOS measurements of  $(\pi^+ + \pi^-)$  [18]. Since the particle ratio of  $\pi^-/\pi^+ \approx 1$  independently of  $p_T$  and centrality (see, e.g., Ref. [2]), the low- $p_T$  values of  $\pi^+$  and  $\pi^-$  spectra have been taken as one-half of  $(\pi^+ + \pi^-)$  reported by PHOBOS. However, some modification of the original PHENIX data [2] has been done to match the PHOBOS data conditions. Namely, the PHOBOS measurements were done for the 15% most central collisions ( $N_{\text{part}} = 303$ ), whereas the PHENIX ones are for the 0–5%, 5–10%, and 10–15% centrality bins. Since the treatment of counts includes the averaging over the number of events in a given centrality bin and for the same run the number of events in the 15% most central bin should be equal to the sum of numbers of events in the 0–5%, 5–10%, and 10–15% centrality bins, the rough approximation of the hypothetical measurement done in the 0–15% centrality bin would be the average of the measurements done in the 0–5%, 5–10%, and 10–15% centrality bins. Such averages have been taken as the PHENIX data for the 0–15% centrality bin. Also, values of the statistical parameters taken for this case are the appropriate averages of the values given for the 0–5%, 5–10%, and 10–15% centrality bins.

As can be seen from the last column of Table I, the best-quality fits have been obtained for the strangeness chemical nonequilibrium case of the SHM. Also, fits done in the chemical equilibrium case are slightly better than those presented for the full chemical nonequilibrium. This conclusion can be expressed in an informal quantifiable way by calculating the average of  $\chi^2/\text{NDF}$  for each case of the SHM.

TABLE I. Values of the geometric parameters of the model for various centrality bins fitted with the use of the PHENIX final data for the  $p_T$  spectra of identified charged hadrons [2]; NDF = 124. For bins with footnotes a and b the data are from Ref. [17]. Values of the statistical parameters are taken from Ref. [1]. The last three rows show the results of fits to the set of data that include the PHENIX data and low- $p_T$   $\pi^+$  and  $\pi^-$  data taken as a half of the PHOBOS data for  $(\pi^+ + \pi^-)$  [18]; here NDF = 132.

Centrality (%)	$N_{\text{part}}$	$T$ (MeV)	$\mu_B$ (MeV)	$\gamma_s$	$\gamma_q$	$\rho_{\text{max}}$ (fm)	$\tau$ (fm)	$\beta_{\perp}^{\text{max}}$	$V_{\text{f.o.}}^{(1)}$ (fm <sup>3</sup> )	$t_{\text{f.o.}}^{(2)}$ (fm)	$\chi^2/\text{NDF}$
0–5	351.4	141.1	25.67	2.430	1.613	$7.24 \pm 0.09$	$6.61 \pm 0.06$	0.74	2177.5	9.8	0.74
5–10	299.0	141.4	24.52	2.367	1.61169	$6.82 \pm 0.08$	$6.17 \pm 0.06$	0.74	1804.4	9.2	0.73
0–10 <sup>a</sup>	325.2	141.25	25.095	2.3985	1.6125	$7.03 \pm 0.08$	$6.39 \pm 0.06$	0.74	1985.8	9.5	0.80
10–15	253.9	141.6	25.27	2.270	1.603	$6.46 \pm 0.08$	$5.81 \pm 0.06$	0.74	1525.6	8.7	0.72
15–20	215.3	140.8	25.05	2.266	1.61497	$6.16 \pm 0.08$	$5.48 \pm 0.05$	0.75	1304.8	8.2	0.85
20–30	166.6	141.0	26.01	2.212	1.61387	$5.58 \pm 0.07$	$4.96 \pm 0.05$	0.75	969.7	7.5	1.24
30–40	114.2	142.0	25.75	2.096	1.608	$4.76 \pm 0.07$	$4.33 \pm 0.05$	0.74	617.0	6.4	1.64
10–40 <sup>b</sup>	171.8	141.35	25.52	2.211	1.61	$5.80 \pm 0.07$	$5.17 \pm 0.05$	0.75	1093.7	7.8	1.28
40–50	74.4	141.7	26.14	2.003	1.605	$4.06 \pm 0.06$	$3.80 \pm 0.04$	0.73	392.6	5.6	2.02
50–60	45.5	141.0	24.05	1.876	1.613	$3.39 \pm 0.06$	$3.32 \pm 0.04$	0.71	239.1	4.7	1.96
60–70	25.7	140.2	25.32	1.636	1.618	$2.72 \pm 0.05$	$2.86 \pm 0.04$	0.69	133.0	3.9	2.16
70–80	13.4	141.7	24.24	1.026	1.299	$2.40 \pm 0.06$	$2.78 \pm 0.05$	0.65	100.6	3.7	1.43
0–5	351.4	154.6	25.04	1.231	1.0	$8.35 \pm 0.10$	$8.57 \pm 0.08$	0.70	3752.1	12.0	0.57
5–10	299.0	155.2	24.73	1.186	1.0	$7.84 \pm 0.10$	$7.97 \pm 0.08$	0.70	3077.1	11.2	0.43
0–10 <sup>a</sup>	325.2	154.9	24.885	1.2085	1.0	$8.10 \pm 0.09$	$8.27 \pm 0.07$	0.70	3407.3	11.6	0.56
10–15	253.9	155.5	26.29	1.169	1.0	$7.37 \pm 0.10$	$7.41 \pm 0.07$	0.70	2527.0	10.4	0.36
15–20	215.3	154.6	25.68	1.147	1.0	$7.07 \pm 0.10$	$7.04 \pm 0.07$	0.71	2212.2	10.0	0.39
20–30	166.6	155.2	27.18	1.121	1.0	$6.37 \pm 0.09$	$6.32 \pm 0.06$	0.71	1609.9	9.0	0.53
30–40	114.2	155.7	27.21	1.080	1.0	$5.47 \pm 0.08$	$5.51 \pm 0.06$	0.70	1036.6	7.8	0.78
10–40 <sup>b</sup>	171.8	155.25	26.59	1.1293	1.0	$6.65 \pm 0.08$	$6.60 \pm 0.06$	0.71	1833.5	9.4	0.53
40–50	74.4	155.5	26.74	1.018	1.0	$4.65 \pm 0.07$	$4.82 \pm 0.06$	0.69	654.6	6.7	1.07
50–60	45.5	152.6	21.62	0.8906	1.0	$4.06 \pm 0.07$	$4.39 \pm 0.06$	0.68	455.2	6.0	1.04
60–70	25.7	152.2	26.12	0.8076	1.0	$3.22 \pm 0.07$	$3.73 \pm 0.05$	0.65	243.0	4.9	1.32
70–80	13.4	148.6	23.82	0.7163	1.0	$2.59 \pm 0.06$	$3.17 \pm 0.06$	0.63	133.6	4.1	1.20
80–92	6.3	150.8	28.00	0.6788	1.0	$1.92 \pm 0.06$	$2.69 \pm 0.06$	0.58	62.3	3.3	1.21
0–5	351.4	155.2	26.4	1.0	1.0	$8.46 \pm 0.10$	$8.84 \pm 0.08$	0.69	3973.4	12.2	0.80
5–10	299.0	155.2	26.4	1.0	1.0	$7.99 \pm 0.10$	$8.23 \pm 0.08$	0.70	3302.6	11.5	0.61
0–10 <sup>a</sup>	325.2	155.2	26.4	1.0	1.0	$8.23 \pm 0.09$	$8.54 \pm 0.07$	0.69	3629.8	11.9	0.80
10–15	253.9	155.2	26.4	1.0	1.0	$7.54 \pm 0.10$	$7.67 \pm 0.08$	0.70	2736.2	10.8	0.48
15–20	215.3	155.2	26.4	1.0	1.0	$7.11 \pm 0.10$	$7.17 \pm 0.07$	0.70	2275.5	10.1	0.48
20–30	166.6	155.2	26.4	1.0	1.0	$6.45 \pm 0.09$	$6.47 \pm 0.07$	0.71	1689.5	9.1	0.58
30–40	114.2	155.2	26.4	1.0	1.0	$5.57 \pm 0.08$	$5.63 \pm 0.06$	0.70	1097.2	7.9	0.77
10–40 <sup>b</sup>	171.8	155.2	26.4	1.0	1.0	$6.74 \pm 0.08$	$6.76 \pm 0.06$	0.71	1932.3	9.6	0.64
40–50	74.4	155.2	26.4	1.0	1.0	$4.68 \pm 0.07$	$4.85 \pm 0.06$	0.69	669.0	6.7	1.05
50–60	45.5	155.2	26.4	1.0	1.0	$3.83 \pm 0.07$	$4.16 \pm 0.05$	0.68	383.9	5.7	1.13
60–70	25.7	155.2	26.4	1.0	1.0	$2.99 \pm 0.06$	$3.47 \pm 0.05$	0.65	194.3	4.6	1.41
70–80	13.4	155.2	26.4	1.0	1.0	$2.22 \pm 0.06$	$2.78 \pm 0.05$	0.62	86.3	3.6	1.55
80–92	6.3	155.2	26.4	1.0	1.0	$1.71 \pm 0.06$	$2.40 \pm 0.05$	0.58	44.2	2.9	1.40
0–15 <sup>c</sup>	303.0	141.4	25.15	2.356	1.609	$6.82 \pm 0.08$	$6.09 \pm 0.05$	0.75	1778.0	9.1	0.87
0–15 <sup>c</sup>	303.0	155.1	25.35	1.195	1.0	$7.87 \pm 0.10$	$8.00 \pm 0.07$	0.70	3111.7	11.2	0.41
0–15 <sup>c</sup>	303.0	155.2	26.4	1.0	1.0	$8.02 \pm 0.10$	$8.26 \pm 0.08$	0.70	3337.0	11.5	0.59

<sup>a</sup>Here statistical parameters are the averages of the parameters listed in two sequential rows above this row.

<sup>b</sup>Here statistical parameters are the averages of the parameters listed in four sequential rows above this row.

<sup>c</sup>Here statistical parameters are the averages of the parameters given for the 0–5%, 5–10%, and 10–15% centrality classes in the same case of the SHM.

So, for the chemical full nonequilibrium  $\langle \chi^2/\text{NDF} \rangle = 1.30$ , for the strangeness chemical nonequilibrium  $\langle \chi^2/\text{NDF} \rangle = 0.77$ , and for the chemical equilibrium  $\langle \chi^2/\text{NDF} \rangle = 0.9$ . Also, the wider range of centrality better fulfills the condition of statistical significance (i.e.,  $\chi^2/\text{NDF} < 1$ ) in both cases

of  $\gamma_q = 1$  (up to 40% of centrality) than in the case of  $\gamma_q \neq 1$  (up to 20% of centrality). Fits done with the inclusion of the low- $p_T$   $\pi^\pm$  measured by PHOBOS have confirmed this conclusion, as can be seen in the last three rows of Table I.

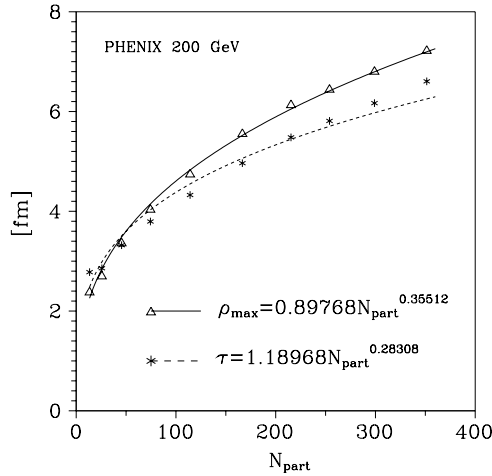


FIG. 1. Values of the geometric parameters of the model from the seventh and eighth column of Table I for the full chemical nonequilibrium case ( $\gamma_s \neq 1$ ,  $\gamma_q \neq 1$ ). The lines are the best power approximations.

Values of the geometric parameters  $\rho_{\max}$  and  $\tau$  from Table I are presented in Figs. 1 and 2 as functions of  $N_{\text{part}}$ . Also, there the lines of the best power approximations are depicted,

$$x \sim N_{\text{part}}^{\kappa}, \quad x = \rho_{\max}, \tau, \quad (24)$$

with scaling exponents  $\kappa \approx 0.36$  for  $\rho_{\max}$  and  $\kappa \approx 0.28$  for  $\tau$ .

### B. Identified hadron spectra

Having obtained parameters of the model we can give the spectra with the use of Eqs. (11) and (12). In Figs. 3 and 4 (top plots) the spectra of sums of negative and positive identified hadrons are depicted. This type of presentation is chosen to

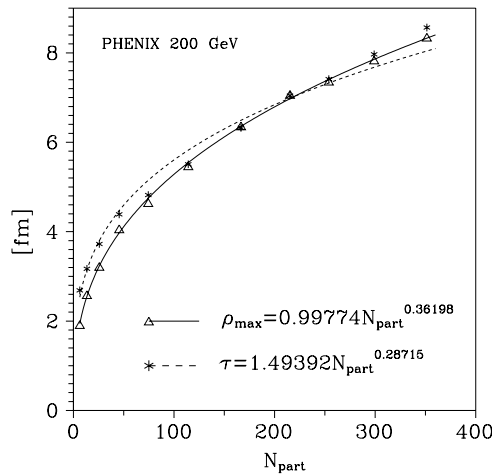


FIG. 2. Values of the geometric parameters of the model from the seventh and eighth column of Table I for the strangeness chemical nonequilibrium case ( $\gamma_s \neq 1$ ,  $\gamma_q = 1$ ). The lines are the best power approximations.

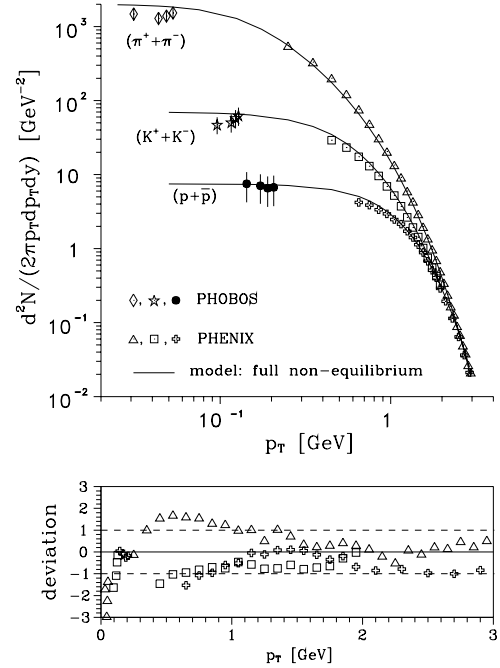


FIG. 3. The top plot presents invariant yields as a function of  $p_T$  for RHIC at  $\sqrt{s_{NN}} = 200$  GeV. The PHOBOS data are for the 15% most central collisions with the error bars expressed as the sum of the systematic and statistical uncertainties [18]. The corresponding PHENIX data [2] are presented as the averages of the invariant yields for 0–5%, 5–10%, and 10–15% centrality bins. For the PHENIX data errors are about 10% and are of the size of the symbols. Lines are the appropriate predictions of the single-freeze-out model for the full chemical nonequilibrium case (fit to the PHENIX data only). The bottom plot shows a deviation of data to the model,  $(f_{\text{exp}} - f_{\text{theor}})/\sigma_{\text{exp}}$ , where  $f_{\text{exp}}(f_{\text{theor}})$  is the experimental (theoretical) value of the invariant yield at given  $p_T$  and  $\sigma_{\text{exp}}$  is the error of  $f_{\text{exp}}$ . Both PHENIX and PHOBOS data are denoted by the same symbol for the same species [i.e., triangles are for  $(\pi^+ + \pi^-)$ , squares for  $(K^+ + K^-)$ , and open crosses for  $(p + \bar{p})$ ].

compare the model predictions for low- $p_T$  values of spectra with the PHOBOS experimental data [18]. Since the PHOBOS data are for the 0–15% centrality bin, the PHENIX data for this bin have been simulated in the same way as explained in Sec. IV A.

In the case of chemical full nonequilibrium (Fig. 3), the low- $p_T$  pions are mostly overestimated ( $\approx 33\%$ ), as are the kaons ( $\approx 21\%$ ), and the best predictions have been made for protons and antiprotons ( $\approx 5\%$  above the data). In the case of chemical strangeness nonequilibrium (Fig. 4), the opposite is true, with pions predicted exactly, but kaons, protons, and antiprotons being overestimated roughly equally ( $\approx 25\%$ ). For the chemical equilibrium case (see Fig. 4 in Ref. [7], which looks almost the same as the top plot of Fig. 4 here) the situation in the low- $p_T$  range is similar to this in the chemical strangeness nonequilibrium case; namely, pions are in complete agreement with the data, kaons are  $\approx 13\%$  above, and protons and antiprotons are the most overestimated ( $\approx 34\%$ ). This discussion confirms the conclusion drawn from the comparison of the values of  $\chi^2/\text{NDF}$ —the chemical

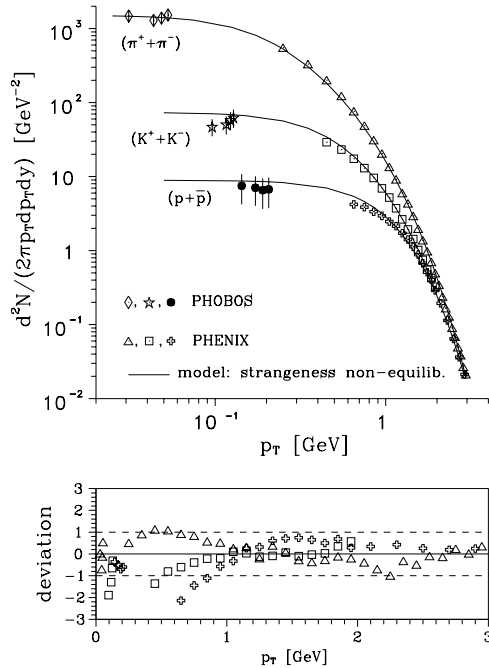


FIG. 4. Same as Fig. 3 but for the strangeness chemical nonequilibrium case.

strangeness nonequilibrium case seems to work in the best way as far as fits to the spectra are concerned.

To visualize the quality of fits and overall predictions, in the bottom plots of Figs. 3 and 4 and in Fig. 5 deviations of data to the model are presented. The deviation is defined as

$$\frac{f_{\text{exp}} - f_{\text{theor}}}{\sigma_{\text{exp}}}, \quad (25)$$

where  $f_{\text{exp(theor)}}$  is the experimental (theoretical) value of the invariant yield at given  $p_T$  and  $\sigma_{\text{exp}}$  is the error of  $f_{\text{exp}}$ . The number of points that are entirely outside of the  $\pm 1$  band is the greatest in the case of chemical full nonequilibrium (21, with most of them corresponding to pions with all the low- $p_T$  sample counted). In both other cases this number is the same and equals 8. Also the widest deviation is in the first case, where it reaches  $-2.9$ , whereas in the case of chemical strangeness nonequilibrium the farthest point is  $-2.1$  and in the chemical equilibrium case  $-2.8$ .

To investigate this problem from the other side, fits for the 15% most central bin have been done with the inclusion of the low- $p_T$   $\pi^\pm$  taken from the PHOBOS data [18]. The data give

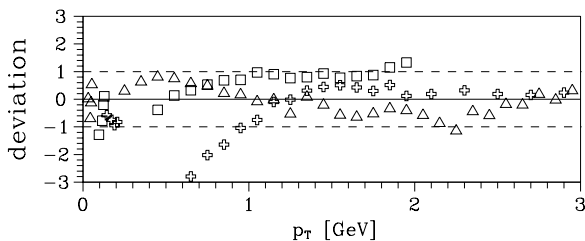


FIG. 5. Same as the bottom plot of Fig. 3 but for the chemical equilibrium case.

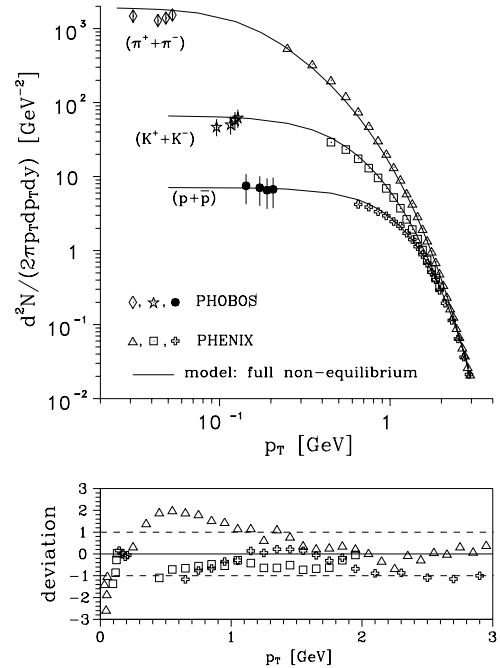


FIG. 6. Same as Fig. 3 but for the simultaneous fit to the PHENIX and low- $p_T$   $\pi^\pm$  PHOBOS data.

values of  $(h^+ + h^-)$  spectra of identified hadrons ( $h = \pi, K, p$ ) at very low  $p_T$ . But only for pions is the particle ratio of  $h^-/h^+ \approx 1$  independently of  $p_T$  and centrality at RHIC (see, e.g., Ref. [2]). Thus values of  $\pi^\pm$  spectra for very low  $p_T$  are taken as one-half of  $(\pi^+ + \pi^-)$  reported by PHOBOS [18]. The results of fits have been gathered in the last three rows of Table I. The corresponding spectra are presented in the top plots of Figs. 6–8. In the bottom plots of Figs. 6–8 deviations of data to the model are depicted. Deviation figures show explicitly what is expressed by the values of  $\chi^2/\text{NDF}$  given in Table I—in the chemical strangeness nonequilibrium case spectra are fitted much better than in both other cases. The number of points outside the  $\pm 1$  band equals 9 in this case and the farthest one is at  $-2.1$  (see the bottom plot of Fig. 7). In the chemical full nonequilibrium case this number is 19 and the farthest point is at  $-2.5$  (see the bottom plot of Fig. 6). In the chemical equilibrium case the number of points outside the  $\pm 1$  band is 8, but one of them reaches the value  $-2.8$  (see the bottom plot of Fig. 8).

From what has been explained so far one can see that the chemical full nonequilibrium freeze-out seems to be less likely in comparison with semi-equilibrium and equilibrium cases. And if  $\gamma_q = 1$  indeed, both these latter cases will be practically undistinguishable; however, semi-equilibrium will be favored.

### C. $\phi$ and $K(892)^{*0}$ spectra

In this section the predictions for the spectra of  $\phi$  and  $K(892)^{*0}$  resonances will be discussed. This is an interesting point since the yields of these resonances measured by the STAR Collaboration [4–6] were used (with the basic yields of the identified hadrons measured by the PHENIX Collaboration

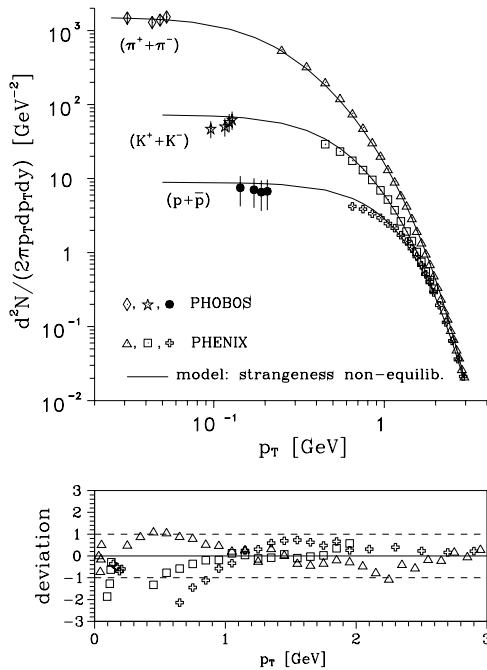


FIG. 7. Same as Fig. 4 but for the simultaneous fit to the PHENIX and low- $p_T$   $\pi^\pm$  PHOBOS data.

[2]) to fit the statistical parameters of the model [1]. In the fitting procedure presented here (to obtain the geometric parameters of the model  $\rho_{\max}$  and  $\tau$ , see Sec. IV A), identified hadron spectra measured by PHENIX [2] have been explored. So the main source of the data used to test the SHM here and in Ref. [1] is the PHENIX measurement at  $\sqrt{s_{NN}} = 200$  GeV. But predictions of the model should be compared with both PHENIX and STAR data, since the STAR data on

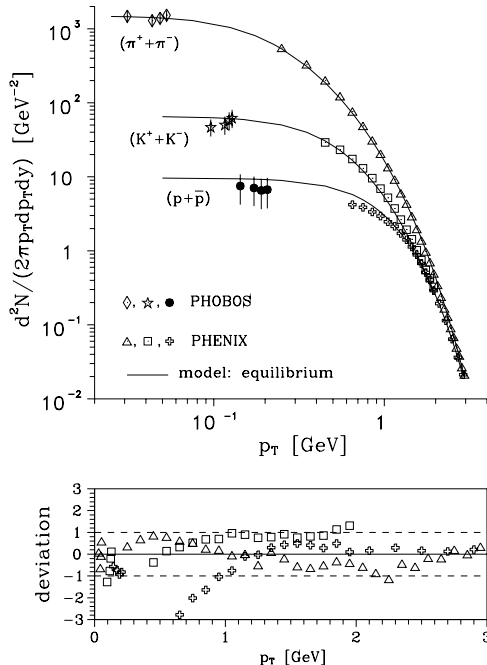


FIG. 8. Same as Fig. 7 but for the chemical equilibrium case.

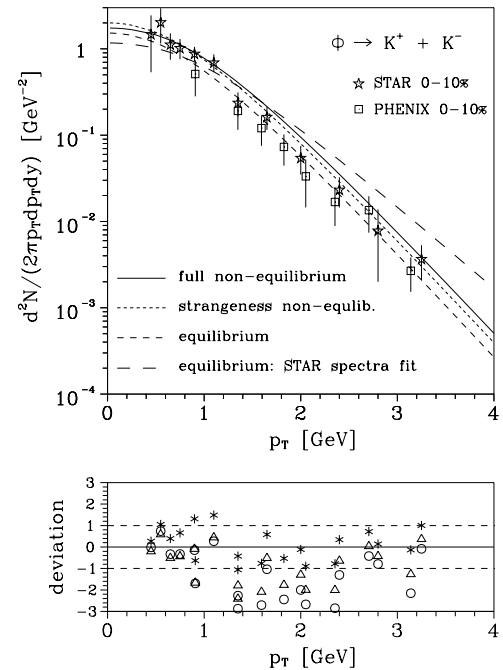


FIG. 9. The top plot presents invariant yields of  $\phi$  mesons measured via the  $K^+K^-$  decay channel as a function of  $p_T$  for the 0–10% centrality bin at  $\sqrt{s_{NN}} = 200$  GeV. Data are from Refs. [6] (STAR) and [17] (PHENIX). The bottom plot shows a deviation of the data to the model predictions based on fits to the PHENIX spectra: chemical full nonequilibrium (circles), strangeness nonequilibrium (triangles), and chemical equilibrium (asterisks).

$K^*(892)/K^-$  and  $\phi/K^-$  ratios were also used in fits of the statistical parameters in Ref. [1]. However, one should keep in mind, when the  $\phi$  spectra are discussed, that the  $\approx 70\%$  difference has been found between  $\phi$  yields at midrapidity measured by STAR [6] and PHENIX [17] for one common centrality bin, 0–10%. The reason for such behavior is still unknown and this is probably not a statistical fluctuation of the lowest  $m_T$  PHENIX point, as suggested in Ref. [1], because when the same  $m_T$  range for both the STAR and the PHENIX  $\phi$  data is considered the difference still persists (see Ref. [59] in Ref. [17]).

In Figs. 9 and 10 predictions for the  $\phi$  production are presented for 0–10% and 10–40% centrality classes of the PHENIX measurement for all three cases of the SHM analyzed here. Additionally, the results for the equilibrium case, but such that the statistical and geometric parameters of the model are fitted to the STAR data only, are also depicted. This is the case considered in Ref. [7]: the statistical parameters ( $T = 160.0$  MeV,  $\mu_B = 24.0$  MeV) are fitted to the STAR particle yield ratios [19] and the geometric parameters to the  $p_T$  spectra of identified hadrons delivered by the STAR Collaboration in Ref. [20]. Again, since the STAR-identified hadron spectra [20] are for different centrality classes than the STAR  $\phi$  spectra [6], the values of geometric parameters for 0–10% and 10–30% centrality bins explored by STAR in  $\phi$ -meson measurements are the averages of the values fitted in Ref. [7] for bins whose added percent coverage equals 0–10% and 10–30%, respectively. This gives  $\rho_{\max} = 8.81$  fm,  $\tau = 6.98$  fm for the 0–10% centrality bin and  $\rho_{\max} = 7.035$  fm,

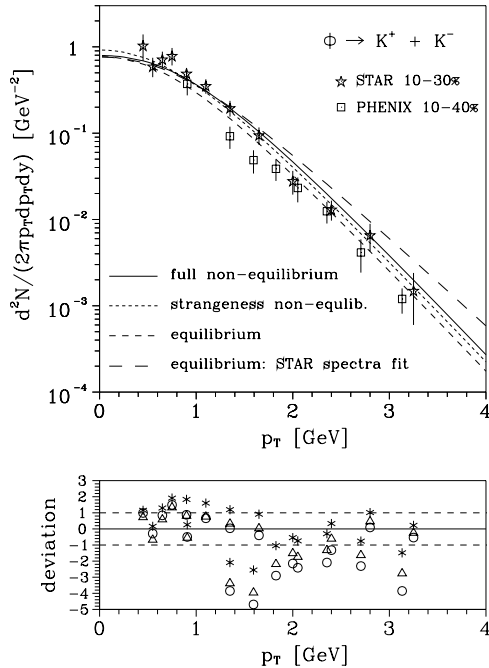


FIG. 10. Same as Fig. 9 but for the 10–40% centrality bin. Note that STAR data are for the 10–30% centrality bin.

$\tau = 6.095$  fm for the 10–30% centrality bin. Results corresponding to these two equilibrium (STAR) cases are presented as long-dashed lines in Figs. 9 and 10. Also, both the PHENIX and the STAR data are depicted in these figures. Note that the STAR second bin is 10–30%, whereas the second PHENIX bin is 10–40% (see Fig. 10). Generally, as one can see in Figs. 9 and 10, all three cases of the SHM agree qualitatively with both the PHENIX and the STAR data when the predictions are based on the fits to the PHENIX spectra (solid, short-dashed, and dashed lines). When the predictions are based on the fit to the STAR spectra (long-dashed lines) they agree with the STAR data only up to the intermediate transverse momentum range and overestimate the high- $p_T$  data. It is not clear why this happens, but within the PHENIX experiment the picture is consistent.

Figures 9 and 10 are on a logarithmic scale, but to see quantitative agreement or disagreement of each SHM case, one should use a linear scale. This has been done in the bottom plots of Figs. 9 and 10, where deviations of both the PHENIX and the STAR data to the model are depicted for all three cases of the SHM considered here. It is clearly seen that predictions in the equilibrium case are substantially better than in both nonequilibrium cases. In fact, both nonequilibrium cases are practically ruled out; however, the strangeness nonequilibrium case seems to behave slightly better than the full nonequilibrium case.

In Fig. 11 results for  $(K^{*0} + \bar{K}^{*0})/2$  spectra are presented together with the STAR data for 0–10% and 10–30% centrality classes [5]. This figure is very instructive since it explicitly shows that the data from different collaborations should not be mixed in any fitting procedure. As one can see, predictions based on fitting to the PHENIX data for the 0–10% centrality class (cf. Table I) are very similar to each other and miss the

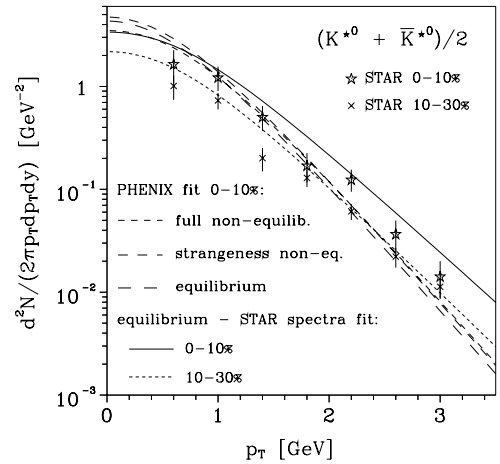


FIG. 11. The invariant yields of  $(K^{*0} + \bar{K}^{*0})/2$  as a function of  $p_T$  for 0–10% and 10–30% centrality bins at  $\sqrt{s_{NN}} = 200$  GeV. Data are from Ref. [5].

STAR data on the  $(K^{*0} + \bar{K}^{*0})/2$  production mainly because of the different slope. In fact, these predictions are above the level of the STAR data for the 0–10% centrality class in the low transverse momenta but they are below even the STAR data for the 10–30% centrality class in the high transverse momenta. Additionally, the results for the equilibrium case, but such that the statistical and geometric parameters of the model are fitted to the STAR data only, are also depicted. This is the case considered in Ref. [7]: The statistical parameters ( $T = 160.0$  MeV,  $\mu_B = 24.0$  MeV) are fitted to the STAR particle yield ratios [19] and the geometric parameters to the  $p_T$  spectra of identified hadrons delivered by the STAR Collaboration in Ref. [20]. Again, since the STAR-identified hadron spectra [20] are for different centrality classes than the STAR  $(K^{*0} + \bar{K}^{*0})/2$  spectra [5], the values of geometric parameters for 0–10% and 10–30% centrality bins explored by STAR in  $(K^{*0} + \bar{K}^{*0})/2$  measurements are the averages of the values fitted in Ref. [7] for bins whose added percent coverage equals 0–10% and 10–30%, respectively. This gives  $\rho_{\max} = 8.81$  fm,  $\tau = 6.98$  fm for the 0–10% centrality bin and  $\rho_{\max} = 7.035$  fm,  $\tau = 6.095$  fm for the 10–30% centrality bin. Results corresponding to these two equilibrium (STAR) cases are presented as solid and shortest dashed lines in Fig. 11. In fact some overestimation in normalization can be seen, mostly in the case of the 0–10% centrality bin, but slopes are correct.

#### D. $\pi^0$ spectra

The occupancy factor  $\gamma_q$ , when it differs from one, could influence the  $\pi^0$  spectra strongly. This is because for  $\pi^0$   $N_q = N_{\bar{q}} = 1$  and  $N_s = N_{\bar{s}} = 0$ . Then in the primordial distribution of  $\pi^0$  one has [see Eq. (9)]

$$\gamma_{\pi^0}^{-1} \exp \left\{ \frac{E_{\pi^0}}{T} \right\} = \exp \left\{ \frac{E_{\pi^0} - \mu_{\pi}}{T} \right\}, \quad (26)$$

where the chemical potential of pions is defined as

$$\mu_\pi = 2T \ln \gamma_q. \quad (27)$$

It has turned out that in the case of chemical full nonequilibrium

$$\mu_\pi \approx m_{\pi^0} \text{ (but } \mu_\pi \leq m_{\pi^0} \text{ always)} \quad (28)$$

for the fitted values of  $\gamma_q$  and  $T$  taken from Ref. [1] and listed in Table I. This means that in this case the values of the statistical parameters happen to hit the critical values for the Bose-Einstein condensation of neutral pions. This has been already stated by the authors of Ref. [1] in Refs. [21,22], namely that if  $\gamma_q$  is freed from 1 but is kept in the range  $[1, \gamma_q^{\text{cr}} = e^{m_{\pi^0}/2T}]$ , it goes to its critical value  $\gamma_q^{\text{cr}}$  during fitting procedure. If this really happened, this could enhance the production of  $\pi^0$ 's with very low  $p_T$ .

Predictions for  $\pi^0$  spectra are presented in Fig. 12 for two nonequilibrium cases of the SHM. The  $\pi^0$  spectrum in the chemical equilibrium case is roughly the same as that for the chemical strangeness nonequilibrium case, so it is not depicted. However, it is impossible to compare the predictions for the

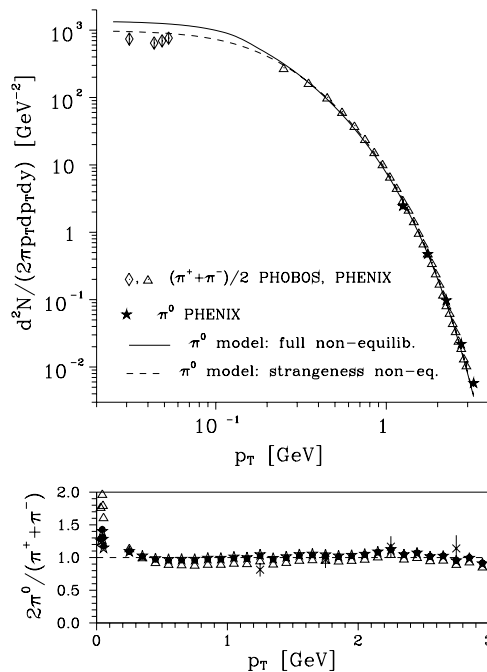


FIG. 12. The top plot presents invariant yields of  $\pi^0$  in comparison with the half of  $(\pi^+ + \pi^-)$  yields for RHIC at  $\sqrt{s_{NN}} = 200$  GeV. The PHOBOS data (diamonds) are for the 15% most central collisions [18]. The corresponding PHENIX data [2] (triangles) are presented as the averages of the invariant yields for the 0–5%, 5–10%, and 10–15% centrality bins. The PHENIX data for  $\pi^0$  (stars) are for the 10% most central bin [23]. For both PHENIX data, errors are about 10% and are of the size of symbols. Lines are the appropriate predictions of the single-freeze-out model. The bottom plot shows a ratio of predicted  $\pi^0$  to the half of measured  $(\pi^+ + \pi^-)$  for the full chemical nonequilibrium case (triangles), the strangeness chemical nonequilibrium case (dots), and the chemical equilibrium case (open stars). Values of the ratio calculated with the use of the experimental data are also depicted (crosses).

low  $p_T$  with the data since the appropriate data are not yet available. Thus in Fig. 12 the comparison is done with the half of the  $(\pi^+ + \pi^-)$  spectrum delivered by PHOBOS for the 15% most central bin [18] and with the corresponding spectrum compiled from the PHENIX data [2]. As is shown in the bottom plot of Fig. 12, the experimental ratio of  $2\pi^0/(\pi^+ + \pi^-) \approx 1$  in the range of  $p_T$  common for  $\pi^\pm$  [2] and  $\pi^0$  [23] PHENIX measurements at  $\sqrt{s_{NN}} = 200$  GeV (i.e., for  $1 < p_T < 3$  GeV).

One can see from the top plot of Fig. 12 that down to  $p_T \approx 0.2$  GeV all three cases of the SHM predict roughly the same spectrum of  $\pi^0$ . (The curve for the chemical equilibrium case is not depicted because, on a logarithmic scale, it would exactly cover the curve for the chemical strangeness nonequilibrium case.) The difference between predictions in the chemical full nonequilibrium case and predictions in both other cases arises at very low transverse momenta and is about 40%. This can be seen very clearly in the bottom plot of Fig. 12, where the ratio of predicted  $\pi^0$  to the half of measured  $(\pi^+ + \pi^-)$  is depicted as a function of  $p_T$  for all three cases of the SHM. The enhancement of neutral pions over one-half of charged pions is  $\approx 80\%$  in the case of chemical full nonequilibrium, whereas for both other cases it is  $\approx 30\%$ . This suggests that the measurement of very low  $p_T$   $\pi^0$ 's could be helpful to judge whether  $\gamma_q \approx \gamma_q^{\text{cr}}$  (as is claimed in Refs. [1,21,22] on the basis of fits to particle yields/ratios) or  $\gamma_q = 1$ .

### E. Transverse energy and charged particle multiplicity estimations

The results of numerical estimations of  $dN_{\text{ch}}/d\eta|_{\text{mid}}$  divided by the number of participant pairs for various centrality classes are presented in Fig. 13 for RHIC at  $\sqrt{s_{NN}} = 200$  GeV. The results are given for two nonequilibrium cases of the SHM. (The estimates in the case of chemical equilibrium are almost the same as in the chemical strangeness nonequilibrium case and have been already presented in Ref. [7]; see Fig. 6 therein.)

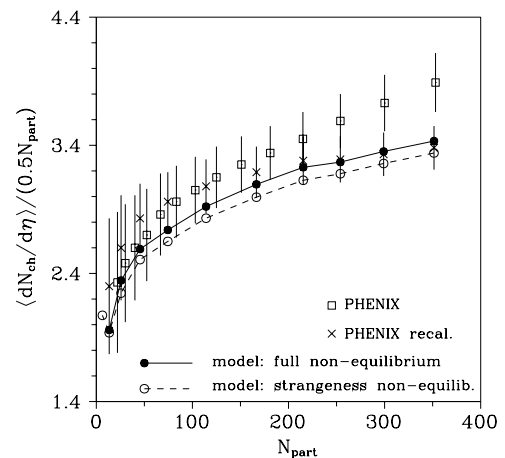


FIG. 13.  $dN_{\text{ch}}/d\eta$  per pair of participants vs  $N_{\text{part}}$  for RHIC at  $\sqrt{s_{NN}} = 200$  GeV. The original PHENIX data are from Ref. [11], whereas the recalculated PHENIX data are from summing the integrated charged hadron yields delivered in Ref. [2]. The lines connect the results and are a guide.

In addition to the straightforward PHENIX measurements of the charged particle multiplicity density, the data from summing the integrated charged hadron yields [2] are depicted in these figures, too. (These data are called “recalculated”; for more explanations see Ref. [7].) Note that the recalculated data differ from the direct ones, especially for more central bins. This has been already noticed by the PHENIX Collaboration (see backup slides of [24]). In Ref. [2] the feeding of  $p(\bar{p})$  from  $\Lambda(\bar{\Lambda})$  decays is excluded. To diminish this effect, integrated  $p$  and  $\bar{p}$  yields delivered in Ref. [2] were corrected to re-include the feeding. The correction was done by division by a factor of 0.65, which is the rough average of a  $p_T$ -dependent multiplier used by the PHENIX Collaboration (see Fig. 4 in Ref. [2] and Eq. (5) therein).

Generally, in both presented cases the model predictions underestimate much more the directly measured  $dN_{\text{ch}}/d\eta|_{\text{mid}}$  than the recalculated  $dN_{\text{ch}}/d\eta|_{\text{mid}}$ . However, the estimates in the chemical full nonequilibrium case are slightly closer to the data and for the four most central bins they agree entirely with the recalculated data points. In the full range of centrality the predictions agree with the recalculated data within errors in this case and almost agree within errors in the chemical strangeness nonequilibrium case. In principle, since the fits of the geometric parameters of the model have been done to the same  $p_T$  spectra here, which were integrated to deliver charged hadron yields in Ref. [2], the predictions for  $dN_{\text{ch}}/d\eta|_{\text{mid}}$  should agree exactly with the recalculated data. However, the transverse momentum spectra are measured in *limited ranges*, so very important low- $p_T$  regions are blank in Ref. [2]. To obtain integrated yields some extrapolations below and above the measured ranges are used. In fact these extrapolations are only analytical fits, but contributions from regions covered by them account for about 25–40% of the integrated yields [25]. These extrapolations could differ from the distributions obtained in the framework of this model and this could be the main source of the discrepancy between the predictions and the recalculated data. So the question of why the significant underestimation of the predicted  $dN_{\text{ch}}/d\eta|_{\text{mid}}$  with respect to the directly measured charged particle multiplicity density occurs should be addressed to the experimentalists: Why does the directly measured  $dN_{\text{ch}}/d\eta|_{\text{mid}}$  differ substantially from the sum of the integrated hadron yields for central collisions?

The values of  $dE_T/d\eta|_{\text{mid}}$  per pair of participants as a function of participant pairs are shown in Fig. 14 for  $\sqrt{s_{NN}} = 200$  GeV. The quality of the model predictions is much better in this case than for  $dN_{\text{ch}}/d\eta|_{\text{mid}}$ ; they agree with the data almost completely. Note that predictions in both presented cases are practically the same and do not differ from the corresponding results in the chemical equilibrium case (see Fig. 7 in Ref. [7]).

Values of the ratio  $\langle dE_T/d\eta \rangle / \langle dN_{\text{ch}}/d\eta \rangle$  as a function of  $N_{\text{part}}$  are presented in Fig. 15. Again, as for  $dN_{\text{ch}}/d\eta|_{\text{mid}}$ , the values predicted in the chemical full nonequilibrium case are slightly closer to the data; they agree with the recalculated data within errors. For the most central bins both sets of predictions agree with the recalculated data within errors. Estimates of  $\langle dE_T/d\eta \rangle / \langle dN_{\text{ch}}/d\eta \rangle$  done within the chemical equilibrium case are practically the same as in the strangeness nonequilibrium case (see Fig. 10 in Ref. [7]). As far as the

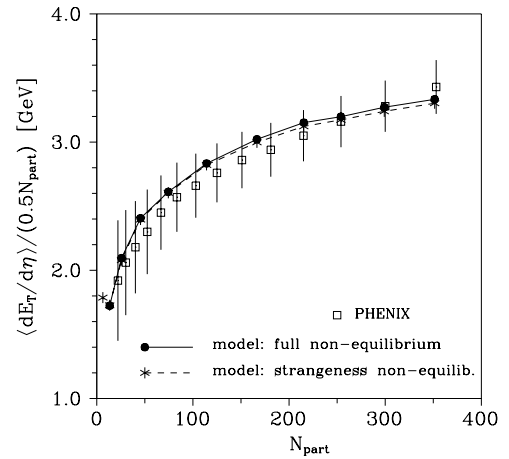


FIG. 14.  $dE_T/d\eta$  per pair of participants vs  $N_{\text{part}}$  for RHIC at  $\sqrt{s_{NN}} = 200$  GeV. The PHENIX data are from Ref. [11]. The lines connect the results and are a guide.

comparison with the direct data [11] is concerned, the position of model predictions is very regular and exactly resembles the configuration of the data in each case, with the estimates being shifted up by only about 10% as a whole.

The last discussed global variable is the total multiplicity of charged particles  $N_{\text{ch}}$ , which can be calculated with the use of Eqs. (22) and (23). The results presented as the total charged particle multiplicity per participating pair versus  $N_{\text{part}}$  are gathered in Fig. 16. Both sets of predictions exhibit almost ideal centrality independence within the range of the PHOBOS measurement, (i.e.,  $N_{\text{part}} \approx 60\text{--}360$ ). Note that in the chemical full nonequilibrium case also normalization agrees almost exactly with the data. In the case of chemical strangeness nonequilibrium a 6% underestimation has resulted, but the predictions still agree with the data within errors. For the

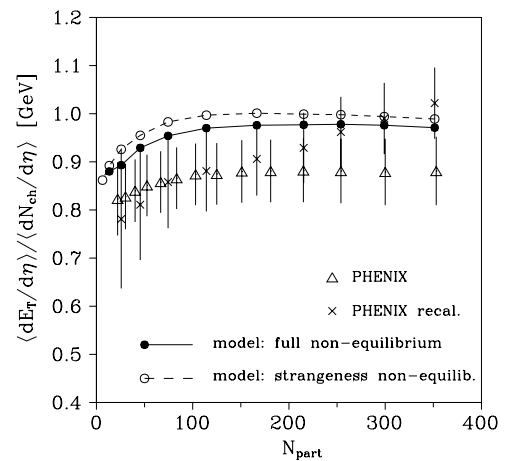


FIG. 15.  $\langle dE_T/d\eta \rangle / \langle dN_{\text{ch}}/d\eta \rangle$  vs  $N_{\text{part}}$  for RHIC at  $\sqrt{s_{NN}} = 200$  GeV. The original PHENIX data are from Ref. [11]. The recalculated PHENIX data are also depicted; here “recalculated” means that the sum of the integrated charged hadron yields [2] has been substituted for the denominator in the ratio. The lines connect the results and are a guide.

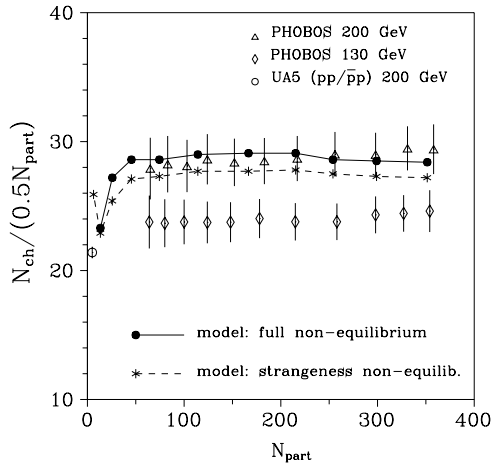


FIG. 16.  $N_{\text{ch}}$  per pair of participants vs  $N_{\text{part}}$  for RHIC at  $\sqrt{s_{NN}} = 200$  GeV. The PHOBOS data are from Ref. [12] and the  $pp/\bar{p}p$  data point of the UA5 measurement is from Fig. 39.5 in Ref. [13]. The lines connect the results and are a guide.

chemical equilibrium similar underestimation was obtained (6.4%; see Fig. 12 in Ref. [7]).

The general conclusion that could be drawn from this discussion is that predictions for global variables agree pretty well with the data in each case of the SHM. However, the chemical full nonequilibrium scenario works slightly better in this respect.

## V. CONCLUSIONS

The extensive analysis of the RHIC data on the particle production in Au-Au collisions at  $\sqrt{s_{NN}} = 200$  GeV has been performed within three possible scenarios of the statistical hadronization model. The SHM explored here is the generalized version of the model of Ref. [1]. The generalization means the explicit inclusion of the fireball expansion in a way as proposed in the single-freeze-out model of Refs. [8–10].

Generally, no definite rejection of any of these scenarios could be done on the basis of this analysis, since different observables prefer different scenarios. However, the chemical full nonequilibrium case seems to be the least likely. This is evident from the studies of particle spectra of stable charged hadrons, both from the statistical significance point of view (values of  $\chi^2/\text{NDF}$  in Table I) and from the behavior of the deviation factor (bottom plots of Figs. 3–8). The  $\phi$ -spectrum test confirms this conclusion (see Sec. IV C). In contrast, the global variable test prefers the full chemical nonequilibrium scenario and does not distinguish between strangeness chemical nonequilibrium and chemical equilibrium cases (see Sec. IV E) but the differences are not significant. The semi-equilibrium and equilibrium scenarios seem to be of similar likelihood, even though the  $\phi$ -spectrum analysis discredits the strangeness chemical nonequilibrium case. This is because the fits to spectra of identified charged hadrons seem to weigh most when the conclusion is to be drawn from the present studies. The  $p_T$  spectra of stable charged hadrons comprise the most numerous and highest quality samples of the experimental

data. For each centrality class of the PHENIX measurement at  $\sqrt{s_{NN}} = 200$  GeV, the  $p_T$ -spectra counts more than 120 points, whereas each sample of the discussed resonance spectra or of the global variable has about 10 points. Moreover, the measurement of a stable charged hadron seems to be more accurate since such a hadron is measured directly whereas resonances can be measured only via their decay products. The last point that supports the relevance of the fits to identified hadron spectra is that all data used in the fitting procedure (here particle yields and  $p_T$  spectra), as well as the data to which predictions are compared, should originate from the same experiment, as has been shown explicitly in Sec. IV C in the example of  $(K^{*0} + \bar{K}^{*0})/2$  spectra (Fig. 11). This is the case of the fits to identified hadron spectra, since the statistical parameters were fitted to the sample comprising six particle yields from PHENIX ( $\pi^\pm$ ,  $K^\pm$ ,  $p$ , and  $\bar{p}$ ) and only two yield ratios from STAR (see Ref. [1]). And with these parameters entering the expression for the invariant distribution, Eq. (11),  $p_T$  spectra of  $\pi^\pm$ ,  $K^\pm$ ,  $p$ , and  $\bar{p}$  measured by PHENIX have been fitted to determine the geometric parameters of the model. Thus the main results presented in Table I have been obtained within practically one experiment (i.e., the PHENIX Collaboration).

This remark should be kept in mind when the SHM predictions for yields of other particles (other than used in the fitting procedure) are compared with the data. For instance, in Ref. [26] predictions for (anti)hyperons were done on the basis of fits from Ref. [1] (i.e., fits done to the data set of which the main part is from PHENIX at  $\sqrt{s_{NN}} = 200$  GeV). However the conclusion is drawn from the comparison with the STAR data at  $\sqrt{s_{NN}} = 130$  GeV. The conclusion is that the chemical full nonequilibrium case is favored. But in the main figure of Ref. [26] (Fig. 2 there), which led to this conclusion, there are no corresponding predictions in the strangeness chemical nonequilibrium case. It is only stated there that these predictions are in between the chemical full nonequilibrium and the chemical equilibrium cases. All these arguments suggest that neither the strangeness chemical nonequilibrium case nor the chemical equilibrium case can be entirely discredited in the context of (anti)hyperon production.

Also, particle yield fluctuations have been proposed as a definite test of what scenario of the SHM is the most likely [27] but one has to await the appropriate data to make a conclusion. This test distinguishes between (semi)equilibrium and nonequilibrium scenarios. What is interesting is that values of the statistical parameters given there for the chemical full nonequilibrium case are again at the condition for the Bose-Einstein condensation of neutral pions,  $\gamma_q \approx \gamma_q^{\text{cr}}$ . (These values are  $T = 140.0$  MeV and  $\gamma_q = 1.62$  [27], which gives  $\mu_\pi = 135.079$  MeV, Eq. (27), so  $\mu_\pi > m_{\pi^0}$  but this is a matter of rounding off [28]; if one takes  $\gamma_q = 1.619$  then  $\mu_\pi < m_{\pi^0}$ .) In fact, as is explained in Refs. [21,22],  $\gamma_q^{\text{cr}}$  is the upper limit of the allowed range of  $\gamma_q$  superimposed before the fitting procedure has started. So by definition  $\gamma_q \leq \gamma_q^{\text{cr}}$  always (if the value of  $\gamma_q$  in a table of Refs. [1,21,22] happens to exceed  $\gamma_q^{\text{cr}}$  this is the result of rounding up [28], as in the aforementioned example). But from the technical point of view, when  $\gamma_q$  slightly exceeds this limit the fitting procedure

will still proceed, since  $\pi^0$  yield is not included in the set of yields and/or ratios to the fit. So the true upper limit should be  $e^{m_{\pi^\pm}/2T}$ , because exceeding this limit causes divergences in primordial densities of  $\pi^+$  and  $\pi^-$ , yields of which are included usually in the set of data to fit. Thus the fitted values of  $\gamma_q$  [1,21,22] seem to be untrustworthy. All these facts put in question the idea of introducing the parameter  $\gamma_q$  into the model. But this supports the conclusion that the chemical full nonequilibrium freeze-out is the least likely. Nonetheless, if values of  $\gamma_q$  were at the critical point for the Bose-Einstein condensation of  $\pi^0$  (as is claimed in Refs. [1,21,22]), then the significant  $\pi^0$  overproduction at low  $p_T$  could happen with respect to one-half of  $(\pi^+ + \pi^-)$  (see Sec. IV D), which seems to be checkable at least in principle.

Our last remark is that the present analysis has been done within a particular hypersurface, as given by Eqs. (1)–(4). Of course, the natural question is to what extent the results depend on the choice of a hypersurface. One of the indirect arguments for this hypersurface are the results of fits to the PHENIX spectra of  $\pi^\pm$ ,  $K^\pm$ ,  $p$ , and  $\bar{p}$  done in Ref. [17] within the very popular blast-wave model [29]. For those fits  $\chi^2/\text{NDF} \approx 3\text{--}4$ , so from the statistical point of view such a hypothesis should be rejected. In contrast, in the present work  $\chi^2/\text{NDF} < 1$  has been obtained for all central and mid-central bins (see Table I).

Thus at least for these bins the hypothesis that the hypersurface has the form as given here cannot be rejected. Moreover, the possible overproduction of low- $p_T$   $\pi^0$ 's seems not to depend very much on a form of the hypersurface chosen since this effect is the result of approaching the condition for the Bose-Einstein condensation of neutral pions. This causes the abrupt increase of the distribution function of  $\pi^0$ ,  $f_{\pi^0}^{\text{primordial}}(p \cdot u)$ , when  $p_T \rightarrow 0$  for all hypersurfaces that have a region with negligible flow.

In summary, in the view of this analysis the chemical full nonequilibrium freeze-out seems to happen least likely during Au-Au collisions at  $\sqrt{s_{NN}} = 200$  GeV and both other cases are of similar likelihood. To help verify this conclusion, the low- $p_T$   $\pi^0$  measurement is proposed since at low  $p_T$  the ratio of  $\pi^0$  over one-half of  $(\pi^+ + \pi^-)$  distinguishes very clearly between  $\gamma_q \approx \gamma_q^{\text{cr}}$  and  $\gamma_q = 1$ .

### ACKNOWLEDGMENTS

The author would like to thank Jan Rafelski and Wojciech Florkowski for very helpful discussions. This work was supported in part by the Polish Committee for Scientific Research under Contract No. KBN 2 P03B 069 25.

- 
- [1] J. Rafelski, J. Letessier, and G. Torrieri, Phys. Rev. C **72**, 024905 (2005).
  - [2] S. S. Adler *et al.* (PHENIX Collaboration), Phys. Rev. C **69**, 034909 (2004).
  - [3] J. Letessier and J. Rafelski, Cambridge Monogr. Part. Phys., Nucl. Phys. Cosmol. **18**, 1 (2002).
  - [4] H. B. Zhang (STAR Collaboration), poster presented at Quark Matter 2004 (QM2004), Oakland, CA, Jan. 11–17, 2004, arXiv:nucl-ex/0403010.
  - [5] J. Adams *et al.* (STAR Collaboration), Phys. Rev. C **71**, 064902 (2005).
  - [6] J. Adams *et al.* (STAR Collaboration), Phys. Lett. **B612**, 181 (2005).
  - [7] D. Prorok, Phys. Rev. C **73**, 064901 (2006).
  - [8] W. Broniowski and W. Florkowski, Phys. Rev. Lett. **87**, 272302 (2001).
  - [9] W. Broniowski and W. Florkowski, Phys. Rev. C **65**, 064905 (2002).
  - [10] W. Broniowski, A. Baran, and W. Florkowski, Acta Phys. Pol. B **33**, 4235 (2002).
  - [11] S. S. Adler *et al.* (PHENIX Collaboration), Phys. Rev. C **71**, 034908 (2005); **71**, 049901(E) (2005).
  - [12] B. B. Back *et al.* (PHOBOS Collaboration), Phys. Rev. C **74**, 021902(R) (2006).
  - [13] K. Hagiwara *et al.* (Particle Data Group Collaboration), Phys. Rev. D **66**, 010001 (2002).
  - [14] D. Prorok, Eur. Phys. J. A **24**, 93 (2005).
  - [15] K. Adcox *et al.* (PHENIX Collaboration), Phys. Rev. Lett. **87**, 052301 (2001).
  - [16] I. G. Bearden *et al.* (BRAHMS Collaboration), Phys. Rev. Lett. **93**, 102301 (2004).
  - [17] S. S. Adler *et al.* (PHENIX Collaboration), Phys. Rev. C **72**, 014903 (2005).
  - [18] B. B. Back *et al.* (PHOBOS Collaboration), Phys. Rev. C **70**, 051901(R) (2004).
  - [19] O. Barannikova (STAR Collaboration), J. Phys. G **31**, S93 (2005).
  - [20] J. Adams *et al.* (STAR Collaboration), Phys. Rev. Lett. **92**, 112301 (2004).
  - [21] J. Rafelski and J. Letessier, Acta Phys. Pol. B **34**, 5791 (2003).
  - [22] J. Letessier and J. Rafelski, submitted to Phys. Rev. C, arXiv:nucl-th/0504028.
  - [23] S. S. Adler *et al.* (PHENIX Collaboration), Phys. Rev. Lett. **91**, 072301 (2003).
  - [24] T. Chujo (PHENIX Collaboration), Nucl. Phys. **A715**, 151 (2003) and <http://alice-france.in2p3.fr/qm2002/Transparencies/20Plenary/Chujo.ppt>.
  - [25] K. Adcox *et al.* (PHENIX Collaboration), Phys. Rev. Lett. **88**, 242301 (2002).
  - [26] J. Letessier and J. Rafelski, Phys. Rev. C **73**, 014902 (2006).
  - [27] G. Torrieri, S. Jeon, and J. Rafelski, Phys. Rev. C **74**, 024901 (2006).
  - [28] J. Rafelski (private communication).
  - [29] E. Schnedermann, J. Sollfrank, and U. Heinz, Phys. Rev. C **48**, 2462 (1993).